Journal of Magnetism and Magnetic Materials 537 (2021) 168104

Contents lists available at ScienceDirect

Journal of Magnetism and Magnetic Materials

journal homepage: www.elsevier.com/locate/jmmm

Research articles

Magnetism and topological Hall effect in antiferromagnetic Ru_2MnSn-based Heusler compounds

Wenyong Zhang [a,b], Balamurugan Balasubramanian [a,b,*], Yang Sun [c], Ahsan Ullah [a,b], Ralph Skomski [a,b], Rabindra Pahari [a,b], Shah R. Valloppilly [a], Xing-Zhong Li [a], Cai-Zhuang Wang [c], Kai-Ming Ho [c], David J. Sellmyer [a,b,*]

[a] Nebraska Center for Materials and Nanoscience, University of Nebraska, Lincoln, NE 68588, USA
[b] Department of Physics and Astronomy, University of Nebraska, Lincoln, NE 68588, USA
[c] Ames Laboratory, U.S. Department of Energy and Department of Physics and Astronomy, Iowa State University, Ames, IA 50011, USA

ARTICLE INFO

Keywords:
Heusler compounds
Antiferromagnetism
Topological Hall effect

ABSTRACT

Heusler compounds and alloys based on them are of great recent interest because they exhibit a wide variety of spin structures, magnetic properties, and electron-transport phenomena. Their properties are tunable by alloying and we have investigated $L2_1$-orderd compound Ru_2MnSn and its alloys by varying the atomic Mn:Sn composition. While antiferromagnetic ordering with a Néel temperature of 361 K was observed in Ru_2MnSn, the Mn-poor $Ru_2Mn_{0.8}Sn_{1.2}$ alloy exhibits properties of a diluted antiferromagnet in which there are localized regions of uncompensated Mn spins. Furthermore, a noncoplanar spin structure, evident from a topological Hall-effect contribution to the room-temperature Hall resistivity, is realized in $Ru_2Mn_{0.8}Sn_{1.2}$. Our combined experimental and theoretical analysis shows that in the $Ru_2Mn_{0.8}Sn_{1.2}$ alloy, the magnetic properties can be explained in terms of a noncoplanar antiferromagnetic scissor mode, which creates a small net magnetization in a magnetic field and subsequently yields a Berry curvature with a strong topological Hall effect.

1. Introduction

Antiferromagnetic materials with small or zero magnetization are of interest for spintronics applications, because they cause little or no fringing fields and may exhibit ultrafast dynamics and interesting magnetotransport properties [1–3]. Antiferromagnets with noncoplanar noncollinear spin structures often show a large topological Hall effect (THE) and manifest magnetic skyrmions, and have therefore attracted much attention in recent years [4–10]. In the case of the non-centrosymmetric ferromagnetic materials including B20-type cubic magnets, the topological properties are usually observed for a limited temperature range immediately below the magnetic transition temperatures [11,12]. By contrast, some antiferromagnets develop non-collinear spin structures from the Néel temperature (T_N) deep into the antiferromagnetic phase at low temperatures [4–8]. For applications, it is important to find magnetic materials that exhibit non-collinear spin structures exhibiting THE and have $T_N > 300$ K. The present paper differs from the usual atomic-scale noncollinearity by investigating a Berry curvature and topological Hall effect of micromagnetic origin, but different from traditional thin-film skyrmions realized on a nanoscale.

Heusler compounds are an important class of materials that show a variety of interesting electronic and magnetic properties including large spin polarization, half metallicity, high anisotropy and magnetization, large anomalous and topological Hall effects, and skyrmion spin structures [13–17]. Our focus is on Ru_2MnSn, which is a full Heusler alloy and whose magnetic properties are intriguing for the following reasons. Theoretical calculations based on full-potential screened Korringa-Kohn-Rostoker Green-function method predict that Ru_2MnSn is a half-metallic ferromagnet exhibiting Slater-Pauling behavior [18]. However, experimentally, Ru_2MnSn is an antiferromagnet with $T_N = 296$ K [19]. These findings suggest that a small perturbation in the electronic structure may have a substantial effect on the magnetic properties of Ru_2MnSn. While Sn is a nonmagnetic element, its electron count often drastically changes the electronic structure and magnetism in Mn-based compounds [20]. In this paper, the Mn to Sn ratio is varied to tailor the magnetic properties of the alloys. Emphasis is on the comparison of the Mn-poor alloy $Ru_2Mn_{0.8}Sn_{1.2}$ with the parent compound Ru_2MnSn, but the Mn-rich composition $Ru_2Mn_{1.2}Sn_{0.8}$ is also considered for reference.

* Corresponding authors.
E-mail addresses: bbalasubramanian2@unl.edu (B. Balasubramanian), dsellmyer@unl.edu (D.J. Sellmyer).

https://doi.org/10.1016/j.jmmm.2021.168104
Received 1 March 2021; Received in revised form 18 April 2021; Accepted 6 May 2021
Available online 13 May 2021

In the Mn-poor alloy, we achieve an antiferromagnetic spin structure that exhibits a noncoplanar spin structure with associated Berry curvature and topological Hall effect.

2. Experimental and computational methods

The alloys were fabricated using the following processing steps. First, high-purity Ru, Mn, and Sn with appropriate amounts were melted using a conventional arc-melting method to produce ingots having the desired compositions. Second, the arc-melted alloys were re-melted to a molten state in a quartz tube and subsequently ejected onto the surface of a water-cooled copper wheel rotating at a speed of 10 m/s to form ribbons of approximate width 2 mm and thickness 70 μm. The details of the melt-spinning method are described in Ref. [21]. Finally, the melt-spun ribbons were sealed in a quartz tube with a base pressure of 3×10^{-6} Torr, annealed at 900 °C for one hour, and then quenched in a cold water to obtain the samples, which were characterized using various techniques.

The structural properties of the polycrystalline alloys were investigated with a *Rigaku Smart Lab X-ray Diffractometer* using Cu K_α radiation of a wavelength of 1.5406 Å and scanning transmission-electron microscope (STEM: *Thermo Fisher Scientific Osiris*). The *TOtal PAttern Solution* (TOPAS) software was used to perform Rietveld analysis on the X-ray-diffraction (XRD) patterns. The composition was measured by energy dispersive x-ray spectroscopy (EDS), using a *Thermo Fisher Scientific* spectrometer attached to the STEM. Magnetic and electron-transport properties were measured using a *Quantum Design Physical Property Measurement System* (PPMS).

First-principles calculations were carried out using the projector augmented wave (PAW) method [22] within density functional theory (DFT) as implemented in the VASP (Vienna *ab initio* Simulation Package) code [23,24]. The exchange and correlation energy were treated within the spin-polarized generalized gradient approximation (GGA) and parameterized by the Perdew-Burke-Ernzerhof formula (PBE) [24]. A plane-wave basis was used with a kinetic energy cutoff of 520 eV. The Monkhorst – Pack's sampling scheme [25] was adopted for Brillouin zone sampling with a *k*-point grid of $2\pi \times 0.025$ Å^{-1}, and the ionic relaxations were stopped when the forces on every atom became smaller than 0.01 eV/Å. The energy convergence criterion is 10^{-5} eV.

3. Results and discussion

This paper focuses on the composition-dependent structural, magnetic, and electron-transport properties of the Ru-Mn-Sn alloys. In this section, we present the structural properties followed by the magnetic and magnetotransport properties. Density-functional theory (DFT) and analytical calculations are used to understand the experimental results on magnetism, magnetoresistance, and topological Hall effect.

3.1. Structural properties

XRD patterns were analyzed by the whole profile-pattern-fitting-method (Rietveld analysis) using Topas v5 software (Bruker AXS) to determine the structure of the Ru_2MnSn-based alloys. The peak intensities are therefore calculated based on the structure factors for the given cell and the respective site occupancies by different atoms. As shown in Fig. 1(a), the experimental XRD patterns of the three alloys are fitted using Rietveld analysis and indexed to the $L2_1$ Heusler structure. The enlarged experimental XRD patterns in the lower-angle region ($2\theta = 21^\circ$ to 34°) also reveal the presence of the (1 1 1) peak as shown in

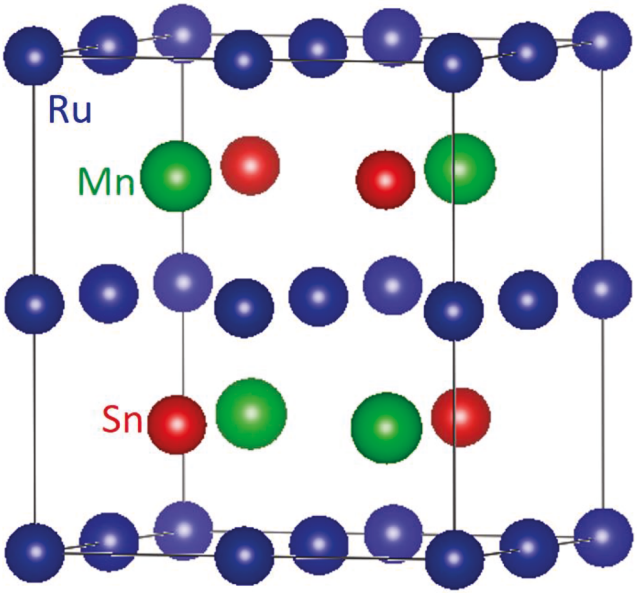

Fig. 2. Unit cell of Ru_2MnSn.

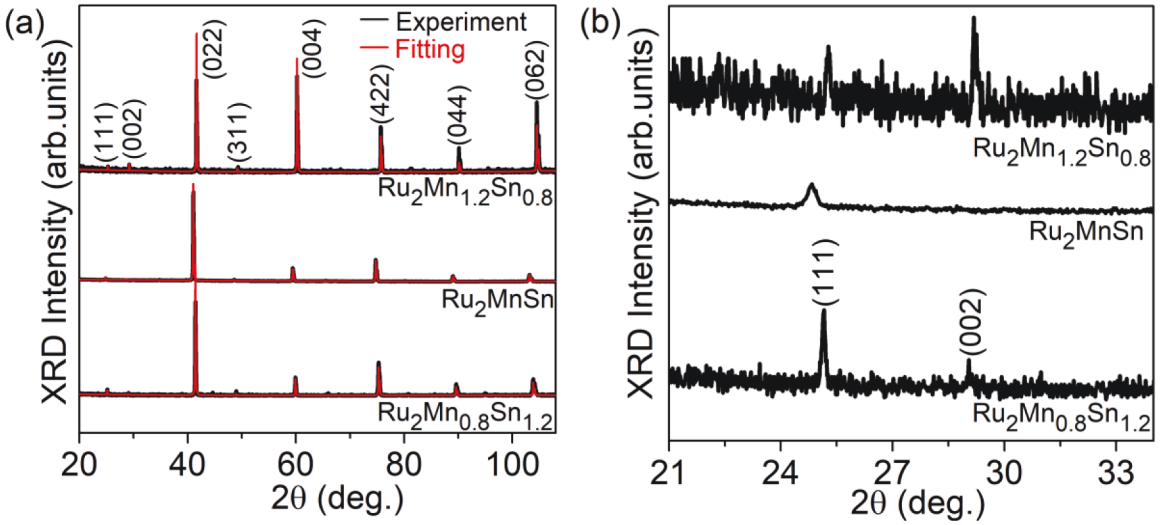

Fig. 1. (a) A comparison of the experimental patterns of $Ru_2Mn_{1.2}Sn_{0.8}$, Ru_2MnSn, and $Ru_2Mn_{0.8}Sn_{1.2}$ (black curves) with the corresponding simulated XRD patterns for the $L2_1$-ordered structure obtained by using Rietveld analysis (red curves). (b) The experimental XRD patterns are enlarged in the 2θ range of 21° to 34° for visualizing the relatively weak (1 1 1) and (0 0 2) diffraction peaks.

Fig. 1(b), and this is a clear indication for the formation of $L2_1$ Heusler structure in these alloys, which is schematically shown in Fig. 2.

As compared to the (1 1 1) diffraction peak, the (0 0 2) diffraction peak is virtually invisible in Ru_2MnSn and exhibit weak intensity in $Ru_2Mn_{0.8}Sn_{1.2}$ (Fig. 1(b)). Note that the (0 0 2) diffraction peak has been observed to become weaker or be completely absent depending on the degree of site disorder in the $L2_1$-ordered Heusler alloys [26]. From simulations, we also observe that the intensity changes of the (1 1 1) and (0 0 2) diffraction peaks of the Ru_2MnSn-based alloys are due to the site disorder between Mn and Sn atoms. About 25% site disorder between Mn and Sn atoms will result in a rather weak (1 1 1) peak and almost negligible (0 0 2) peak. This is quite similar to what we observed in the cases of Ru_2MnSn and $Ru_2Mn_{0.8}Sn_{1.2}$.

By contrast, for the $Ru_2Mn_{1.2}Sn_{0.8}$ sample, the (0 0 2) and (0 0 4) XRD peaks are relatively stronger than the corresponding XRD peaks of the other two samples. This is likely due to texture in the sample, which was also included in the Rietveld analysis. In brief, Rietveld fittings are consistent with the occupancies of excess Sn on Mn sites and Mn on Sn sites in the Mn-poor and Mn-rich alloys, respectively. In addition, XRD patterns rule out the detectable presence of secondary phase in these alloys, within the detectable limit of about 1 wt%. Fig. 1(b) also shows a shift in the peak position of the diffraction peaks towards higher angle side in $Ru_2Mn_{0.8}Sn_{1.2}$ and $Ru_2Mn_{1.2}Sn_{0.8}$ as compared to Ru_2MnSn. This result is consistent with slightly lower lattice parameters obtained using Rietveld analysis for $Ru_2Mn_{0.8}Sn_{1.2}$ ($a = 6.1902$ Å) and $Ru_2Mn_{1.2}Sn_{0.8}$ ($a = 6.1625$ Å) as compared to Ru_2MnSn ($a = 6.2178$ Å).

Transmission-electron microscopy (TEM) also confirms the $L2_1$ Heusler structure of the alloys. For example, Fig. 3 shows a TEM image (a) and the corresponding electron diffraction pattern measured along the [0 0 1] zone axis (b) for $Ru_2Mn_{1.2}Sn_{0.8}$. The experimental electron diffraction pattern is in good agreement with the simulated pattern (not shown here), which was obtained by using the Landyne-SAED3 software [27] and assuming the $L2_1$ Heusler structure. The composition determined using EDS for the sample is $Ru_{1.99}Mn_{1.22}Sn_{0.79}$, very close to the nominal composition $Ru_2Mn_{1.2}Sn_{0.8}$.

3.2. Magnetic properties

Fig. 4 shows the magnetizations of the three alloys as a function of temperature (a) and field (b). The blue curve in (a) shows that the $Ru_2Mn_{1.2}Sn_{0.8}$ has a nonzero spontaneous net magnetization or 'saturation magnetization' M_s below the Curie temperature $T_c = 310$ K, meaning that the basic spin structure of the alloy is ferromagnetic-like (FM). The spontaneous magnetization of this Mn-rich sample is fairly high, about 400 emu/cm^3, which corresponds to 2.52 μ_B per formula unit (f.u), and the low-temperature coercivity is about 0.38 kOe [Fig. 4 (b)].

The other two samples have much lower magnetizations in a field of 1 kOe, namely about 0.08 emu/cm^3 (Ru_2MnSn) and 0.4 emu/cm^3 ($Ru_2Mn_{0.8}Sn_{1.2}$) at 10 K [Fig. 4(a)]. This plus the low magnetization in Fig. 4(b) suggests that the spin structures are basically antiferromagnetic (AFM). The stoichiometric sample (green) shows a maximum at an apparent Néel temperature of 361 K [Fig. 4(a)]. There is another maximum around 50 K, reminiscent of similar unexplained maxima in Ru_2MnZ (Z = Sn, Si, Sb) [19]. However, a comparison of the blue and green curves in Fig. 4(a) shows that the additional peak in the stoichiometric sample (green) mirrors the main FM signal of Mn-rich alloy (blue). This indicates the presence of a tiny fraction of a FM impurity phase, which becomes visible due to the very small magnetization of the main AFM phase. Based on the magnetizations of $Ru_2Mn_{1.2}Sn_{0.8}$ [blue curve in Fig. 4(a)] and Ru_2MnSn [green curve in Fig. 4(a)] at low temperatures (around 10 K), the FM impurity phase in Ru_2MnSn was estimated to be about 0.03 vol%. Note that this secondary phase was not detectable using XRD and TEM due to the very small fraction.

The Mn-poor sample has a very small magnetization and does not show any clear magnetic phase-transition signatures. While such a low magnetization may also indicate that the sample is nonmagnetic (paramagnetic), this explanation is unlikely because of relatively high slope of the red curve in Fig. 4(b). By considering the AFM state of Ru_2MnSn, the Mn-poor sample is likely to be basically AFM, but with a deficiency of Mn atoms on sites occupied in the parent compound. Thus, the magnetic structure very likely can be described as a "diluted" AFM in which there are localized regions or clusters of uncompensated Mn spins. This would account for the increase in magnetization and susceptibility of the $Ru_2Mn_{0.8}Sn_{1.2}$ sample as compared to the Ru_2MnSn sample, as seen in Fig. 4. The evidence for a magnetic transition is rather weak but may be associated with the weak shoulder at 310 K seen in the inset of Fig. 4(a), and such a weak transition or shoulder instead of a peak corresponding to T_N also has been observed in Pt_2MnGa due to the presence of a small ferromagnetic component [28]. The "frozen" uncompensated spins could account for the hysteresis seen in Fig. 4(b). This picture of a weakened intersublattice exchange in the diluted $Ru_2Mn_{0.8}Sn_{1.2}$ sample is consistent with the enhanced THE seen in the sample discussed below (Fig. 7).

In order to understand the magnetism of the Ru-Mn-Sn alloys, we have performed DFT calculations for the parent Ru_2MnSn compound, considering the FM and AFM spin configurations shown in Fig. 5(a) and (b), respectively. The spin configuration of Fig. 5(b) corresponds to the AFM type-2 structure, which has been shown to exist in Ru_2MnX compounds (X = Ge, Sn, Sb) by neutron diffraction [19]. The respective total energies of the FM and AFM configurations are very close, –7.9034 and –7.8977 eV per atom, but our experiments show that Ru_2MnSn is AFM.

By considering a very small difference between the total energies of FM and AFM states (about 0.0057 eV/atom), it is also not surprising to see FM in $Ru_2Mn_{1.2}Sn_{0.8}$. As mentioned earlier, a small perturbation in the electronic structure due to Sn deficiency or excess Mn presumably creates FM in $Ru_2Mn_{1.2}Sn_{0.8}$. DFT calculations yield a net magnetic moment of 3.01 μ_B/f.u for the FM structure, which follows the N_v – 24

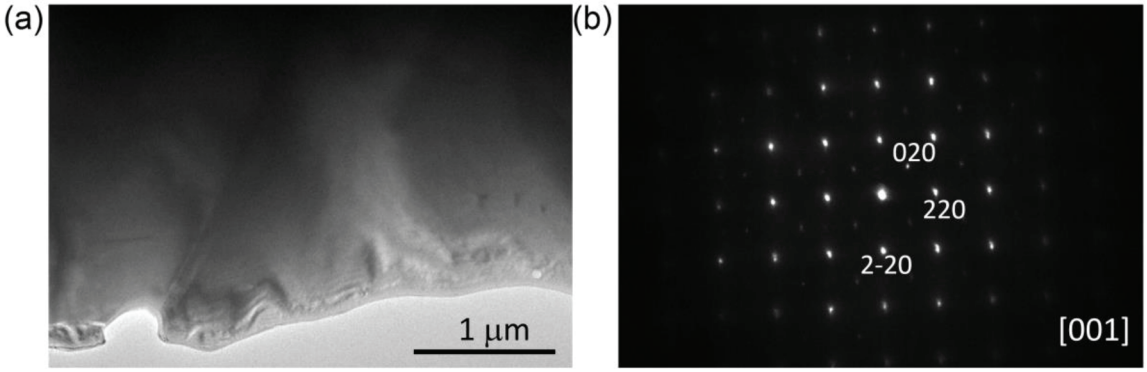

Fig. 3. Structure of $Ru_2Mn_{1.2}Sn_{0.8}$: (a) TEM image and (b) the corresponding diffractogram indexed to the $L2_1$-ordered structure along the [0 0 1] zone axis.

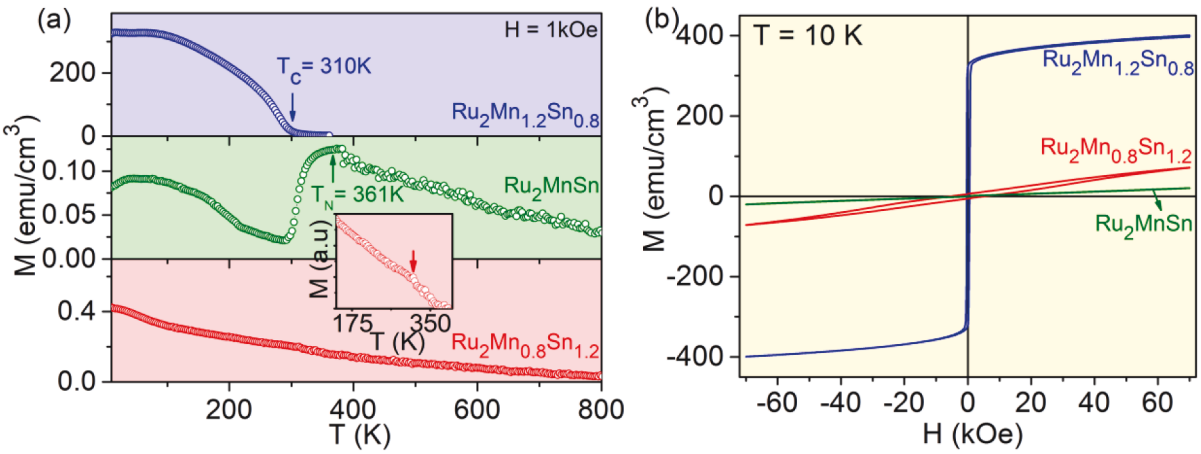

Fig. 4. Magnetic properties: (a) temperature-dependence of the magnetization in a field of 1 kOe and (b) field dependence of the magnetization measured at 10 K. Note the greatly reduced vertical scales in the green and red parts of (a). The inset in (a) shows the $M(T)$ curve of the $Ru_2Mn_{0.8}Sn_{1.2}$ alloy indicating a slope change or very weak shoulder around 310 K (see the text for details).

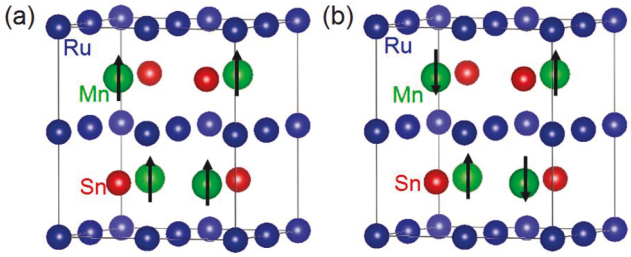

Fig. 5. Unit cells showing the two Ru_2MnSn spin configurations considered in the DFT calculations: (a) ferromagnetic (FM) and (b) antiferromagnetic (AFM).

Slater-Pauling rule (N_v is the number of valence electrons) and is also comparable with the experimental value observed for $Ru_2Mn_{1.2}Sn_{0.8}$ (2.54 μ_B/f.u). Each Mn atom in the AFM structure exhibits a magnetic moment of about 3.27 μ_B shown by DFT calculations, but the net magnetic moment of the system is zero.

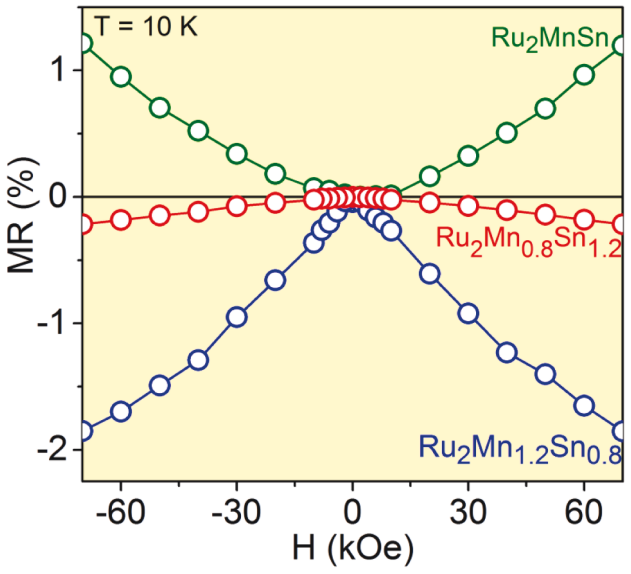

Fig. 6. Magnetoresistance measured at 10 K.

3.3. Magnetoresistance and topological Hall effect

Fig. 6 shows the field dependence of magnetoresistance (MR) for the three compositions. The Mn-rich alloy exhibits the negative magnetoresistance typical of ferromagnets, caused by spin alignment in the magnetic field [29]. The MR of the parent alloy Ru_2MnSn is positive, as

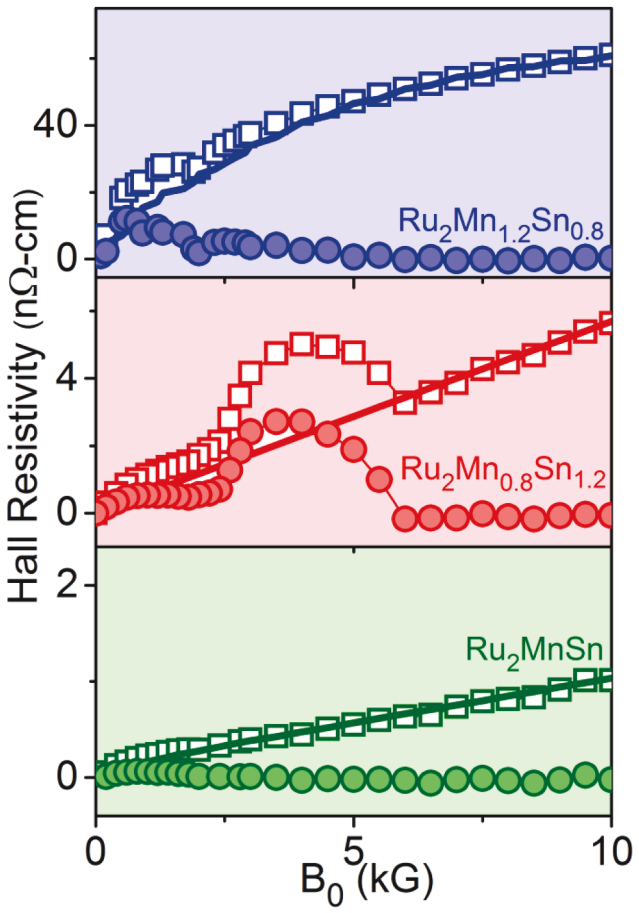

Fig. 7. Hall effect at 300 K: field dependences of the Hall resistivity ρ_{xy} (open squares) and of the topological Hall effect (filled circles) as a function of external magnetic field $B_0 = H$ in kG (cgs) or $\mu_0 H$ in T (SI). The solid curves are the Hall resistivities without the topological Hall-effect term.

expected for antiferromagnets, where the field has the effect of enhancing rather than reducing the misalignment [29,30]. The Mn-poor AFM alloy $Ru_2Mn_{0.8}Sn_{1.2}$ (red) exhibits a weakly ferromagnetic MR signature, which is probably related to the relatively high slope of the red curve in Fig. 4(b) and due to the pronounced scissor mode described below.

Fig. 7 shows the field dependence of the Hall resistivity $\rho_{xy}(B_0)$ at 300 K (open squares). $B_0 = H$ in kG (cgs) or $\mu_0 H$ in T (SI) is an external magnetic field. The Hall resistivity is often expressed as $\rho_{xy} = \rho_{OH} + \rho_{AH} + \rho_{THE}$, where $\rho_{OH} = R_0 B_0$, $\rho_{AH} = 4 \pi M R_s$, and ρ_{THE} are the ordinary, anomalous and topological Hall-effect contributions, respectively. In these equations, R_0 is the ordinary Hall coefficient and R_s are the anomalous one.

Following the standard procedure from the literature [31–33], R_o and R_s have been determined from the high-field $\rho_{xy}(B_0)$ data and used to extract the THE contribution $\rho_{THE} = \rho_{xy} - \rho_{OH} - \rho_{AH}$ (filled circles in Fig. 7). The bumps in the Hall-effect and THE curves are characteristic of the topological Hall effect caused by the Berry curvature. This curvature is realized in noncoplanar spin structures, which are common in skyrmionic thin films [34,35] but also occurs in other micromagnetic systems [33]. Pictorially, conduction electrons (or holes) change their spin direction due to the exchange interaction with the lattice spins, and the corresponding spin rotation translates into a Berry curvature and into an emergent magnetic field that contributes to the Hall effect.

The Mn-poor sample exhibits a particularly large THE (red curve in Fig. 7), which requires a physical explanation. The topological Hall effect in ordinary antiferromagnets is expected to be virtually zero, as it is the case for Ru_2MnSn (green curve in Fig. 7). It is well-known that certain noncoplanar atomic-scale noncollinearities give rise to a substantial THE in the absence of a magnetic field, but there is no evidence for such spin configurations in the present system, and the zero-field THE is zero. In other words, a small external magnetic field of about 5 kG [0.5 T] is sufficient to create a substantial THE, which cannot be explained as an atomic phenomenon involving the electronic structure.

Our explanation is that the THE involves the antiferromagnetic scissor mode, which is schematically shown in Fig. 8(b). The propeller mode of Fig. 8(a), which amounts to a rotation of the Néel vector $\boldsymbol{N} = \boldsymbol{M}_A - \boldsymbol{M}_B$, is easy to create, for example by the random anisotropy associated with the polycrystallinity of the samples. Conduction electrons of a given spin interact differently with the ↑ (blue) and ↓ (red) spins of the propeller mode, which gives rise to a substantial *spin* Hall effect [34], but the net spin polarization of an antiferromagnet is zero, so that the propeller mode does not contribute to the THE.

The scissor mode, explained in Fig. 8(b), is well-known to exist in antiferromagnets and creates a small net magnetization $\boldsymbol{M} = \boldsymbol{M}_A + \boldsymbol{M}_B$, as schematically shown in Fig. 8(c). The new physics investigated in this study is that any spatial variation of this mode yields a Berry curvature similar to that created by ferromagnets. The corresponding integral Berry curvature or topological Hall effect is of the form [35]

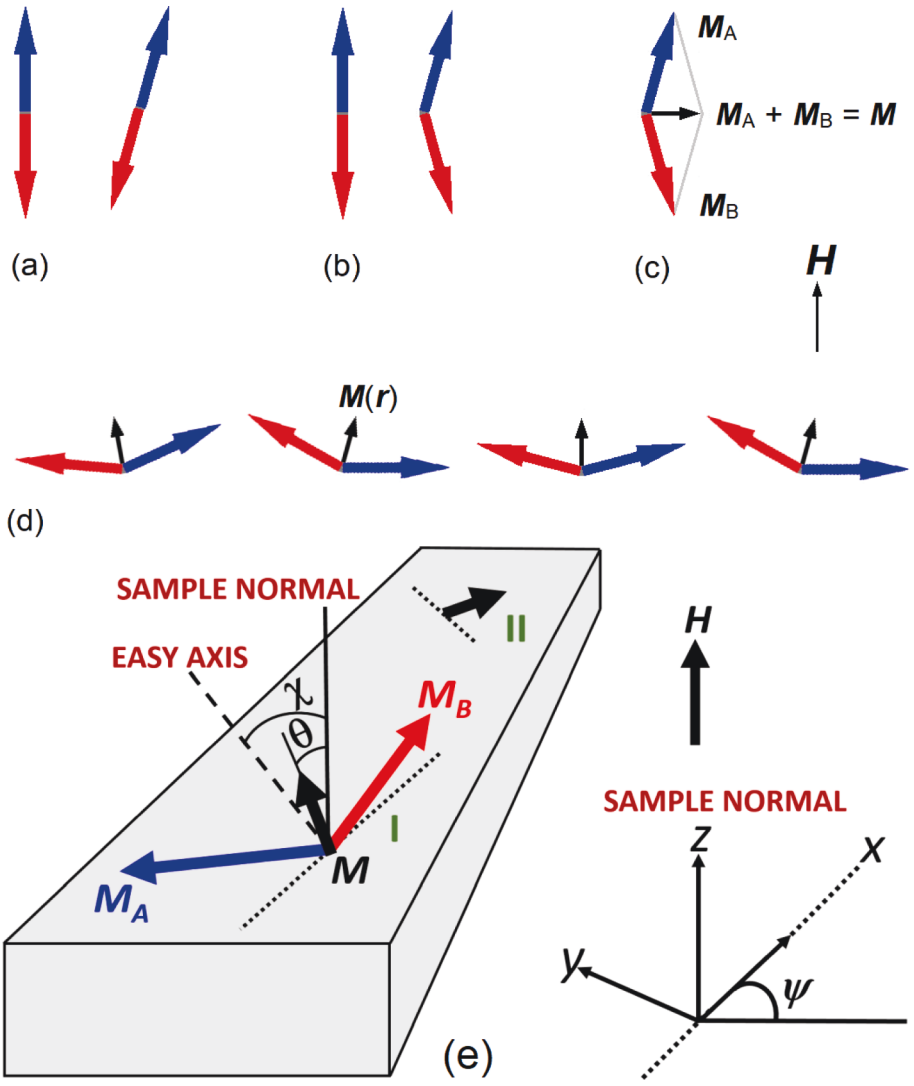

Fig. 8. Antiferromagnetic (AFM) magnetization modes: (a) propeller mode, (b) scissor mode, (c) net magnetization, and (d) schematic situation in a random-anisotropy antiferromagnets subjected to a magnetic field, and (e) coordinate frames used in the paper. The field $\boldsymbol{H}$ is perpendicular to the sample plane (ribbon plane, x-y-plane) and the angle between $\boldsymbol{H}$ and $\boldsymbol{M}$ is θ. The angles χ and ψ are the angles between easy axis and the sample normal and the in-plane rotation angle of the coordinate frame, respectively. The local magnetizations are in the planes created by the dashed and dotted lines, and these planes are different in different regions (I, II). The noncoplanarity of $\boldsymbol{M}(\mathbf{r})$, which gives rise to the THE, is epitomized by the two different directions of the black net-magnetization arrows in Regions I and II giving rise to noncoplanarities.

$$Q = \frac{1}{4\pi}\int \boldsymbol{M}\hat{\mathrm{A}}\cdot\left(\frac{\partial \boldsymbol{M}}{\partial x}\times\frac{\partial \boldsymbol{M}}{\partial y}\right)dV \tag{1}$$

The question is why the THE is big in the Mn-poor alloy but small in the stoichiometric alloy, both being antiferromagnets. The answer is provided by the magnitude of the net magnetization, $|\boldsymbol{M}| \ll M_s$, where $M_s = |\boldsymbol{M}_A| = |\boldsymbol{M}_B|$ is the sublattice magnetization. The magnitude scales as $\mu_o\mu_B H/J^*$ [36], where $J^* = |J_{AB}|$ is the antiferromagnetic intersublattice exchange. Exchange fields (J^*/μ_B) are typically of the order of several 100 T and therefore much higher than typical applied fields, for example $\mu_o H \leq 1$ T ($B_0 = 10$ kG) in Fig. 7. As a consequence, the antiferromagnetic THE is expected to be rather small.

The determination of the net magnetization $\boldsymbol{M}(\boldsymbol{r})$ is nontrivial and involves the external magnetic field H, the strength (K) and local direction ($\boldsymbol{n}$) of the magnetocrystalline anisotropy, the intersublattice exchange J*, and the intrasublattice exchange stiffness (see Ref. [37] and references therein). We assume that the crystallite or grain size is much larger than $(A/K)^{1/2}$, so that the zero-field spin structure is determined by $\boldsymbol{n}$, which obeys $|\boldsymbol{n}| = 1$. Let us consider the quasiclassical model Hamiltonian

$$\mathrm{H} = \mu_o \mathbf{M}_A\cdot\mathbf{H} - \mu_o \mathbf{M}_B\cdot\mathbf{H}\frac{K}{M_s^2}\left[(\mathbf{M}_A\cdot\mathbf{n})^2 + (\mathbf{M}_B\cdot\mathrm{n})^2\right] + J*\mathbf{M}_A\cdot\mathbf{M}_B \tag{2}$$

Since $\boldsymbol{M}_A = ½(\boldsymbol{M} + \boldsymbol{N})$ and $\boldsymbol{M}_B = ½(\boldsymbol{M} - \boldsymbol{N})$ yield $\boldsymbol{M}_A\cdot\boldsymbol{M}_B = ½\boldsymbol{M}^2 - M_s^2$ and

$$M^2 + N^2 = 4M_s^2 \tag{3}$$

Eq. (2) simplifies to

$$\mathrm{H} = \mu_o \mathbf{M}\cdot\mathbf{H}\frac{K}{2M_s^2}\left[(\mathbf{M}\cdot\mathbf{n})^2 + (\mathbf{N}\cdot\mathbf{n})^2\right] + 1/2J*\left(\mathrm{M}^2 - 2\mathrm{M}_s^2\right) \tag{4}$$

Let us apply a field in the z-direction and consider a grain or crystallite with arbitrary easy-axis direction $\mathbf{n}$. By rotating the coordinate frame in the x-y plane (rotation angle ψ), we can move the easy axis into the x-z-plane, or paper plane in Fig. 8(e). The easy-axis vector is then $\boldsymbol{n} = \cos\chi\,\boldsymbol{e}_z + \sin\chi\,\boldsymbol{e}_x$, where χ is the angle between easy axis and sample normal. This means that the net magnetization is also in the x-z-plane, $\boldsymbol{M} = M(\sin\theta\,\boldsymbol{e}_x + \cos\theta\,\boldsymbol{e}_z)$ and that the Néel vector, which is perpendicular to $\boldsymbol{M}$, obeys $\boldsymbol{N} = N(\cos\theta\,\boldsymbol{e}_x - \sin\theta\,\boldsymbol{e}_z)$.

Equation (4) contains two independent variables, and it is convenient to choose the magnitude M and the angle θ of the net magnetization; the length N of the Néel vector is not independent but implicitly given by Eq. (3). Equation (4) then becomes

$$\mathscr{H} = --\mu_o\mathrm{H}\cdot\mathrm{M}\cos\theta + \mathrm{K}\cos(2\theta - -2\chi) + \mathrm{J}*\mathrm{M}^2 \tag{5}$$

where we have ignored a physically unimportant zero-point energy and taken into account that $M \ll M_s$.

Minimization of Eq. (4) with respect to M and θ yields the magnitude of the net magnetization

$$M = \frac{\mu_o\mu_B H}{J^*}\cos(\theta) \tag{6}$$

and the nonlinear equation

$$\frac{\mu_o^2 H^2}{4KJ^*}\sin(2\theta) = \sin(2\theta - 2\chi) \tag{7}$$

This equation has two solutions, namely

$$\theta = \frac{1}{2}\mathrm{atan}\left(\frac{\sin(2\chi)}{(H/H_{SF})^2 - \cos(2\chi)}\right) \tag{8a}$$

and

$$\theta = \frac{\pi}{2} - \frac{1}{2}\mathrm{atan}\left(\frac{\sin(2\chi)}{(H/H_{SF})^2\cos(2\chi)}\right) \tag{8b}$$

here $H_{SF} = (4KJ^*)^{1/2}/\mu_o$ is the spin-flop field, and it can be shown that the two solutions actually reproduce the spin-flop transition [36]. In term of Fig. 8, these transitions amount to rotation of the two spin sublattices by 90°, from (b) to (d).

The present scenario, schematically shown in Fig. 8(d), is described by Eq. (8a). In the high-field limit, the angle θ is small and obeys

$$\theta(\mathrm{r}) = \frac{H_{SF}^2}{2H^2}\sin(2\chi(\mathrm{r}))\,) \tag{9}$$

By symmetry, θ is zero for $\chi = 0$ (easy axis parallel to external field) and for $\chi = 90°$ (easy axis perpendicular to external field). The angle θ reaches a maximum at $\chi = 45°$ and ensemble-averaging over all random easy-axis directions yields $<\sin^2(2\chi)> = 8/15$, corresponding to $<\theta> = 0.3651\,H_{SF}^2/H^2$. For $\chi = 45°$, Eq. (8a) simplifies to $\theta = -½\,\mathrm{atan}(H_{SF}^2/H^2)$; this function is shown in Fig. 9 (dashed line).

Equation (1) shows that the THE scales as M^3. However, this is not the only consideration. In very high fields, Eq. (9) predicts $\theta \approx 0$ for all easy-axis misalignments, so that all spins are oriented in the field direction and the gradients in Eq. (1) vanish. Furthermore, the spins must be not only noncollinear but also noncoplanar. Equation (1) is a continuum version of the requirement to have local magnetizations $\boldsymbol{M}_1$, $\boldsymbol{M}_2$, and $\boldsymbol{M}_3$ so that $\boldsymbol{M}_1\cdot(\boldsymbol{M}_2 \times \boldsymbol{M}_3) \neq 0$. Random anisotropy satisfies this requirement, because the in-plane rotation angle ψ is different for each grain. The magnetization distribution in the grains is not known, but in fair approximation we can consider three spins characterized by common values of M and θ while having $\psi_1 = 0°$, $\psi_2 = 120°$, and $\psi_3 = 240°$, respectively. Evaluation of the cross product shows that the THE is proportional to

$$M_1\cdot(M_2 \times M_3) = \frac{3\sqrt{3}}{2}\,M^3 cos\theta\, sin^2\theta \tag{10}$$

where M is given by Eq. (6) and θ by Eq. (8a). The solid line in Fig. 9 shows the field dependence of this expression for $\chi = 45°$.

The THE curve in Fig. 9 exhibits a maximum at $H = 1.409\,H_{SF}$. The spin-flip field is the geometric mean of the (sublattice) anisotropy field and exchange field, and both quantities vary greatly across materials. However, 0.5 T $< \mu_o H_{SF} <$ 5 T is a typical range, and we expect the THE maximum to be roughly in this region. Unfortunately, the anisotropy of the present alloys is unknown and difficult to determine, also because the present material are cubic and the uniaxial anisotropy in Eq. (2) is a qualitative rather than quantitative approximation. To explain the difference between Ru_2MnSn and $Ru_2Mn_{0.8}Sn_{1.2}$ in Figs. 4 and 6, we take into account that J* changes substantially with increasing Sn concentration. This feature follows from Fig. 4(a) to 4(b), which show that the susceptibility dM/dH of $Ru_2Mn_{0.8}Sn_{1.2}$ is nearly 6 times higher than that

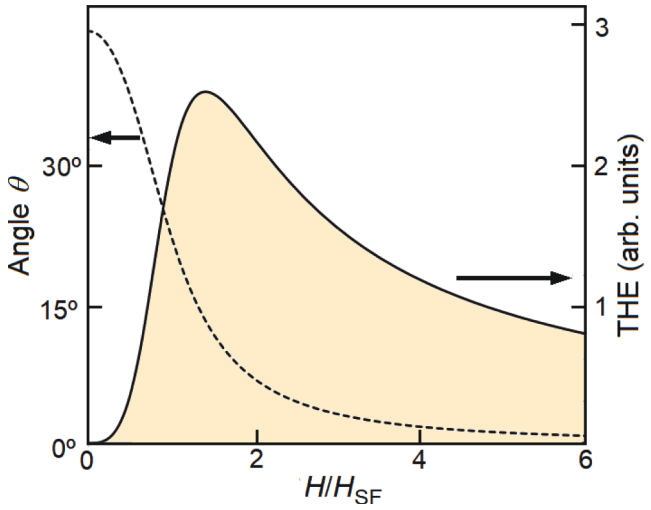

Fig. 9. Misalignment angle and topological Hall effect.

of Ru_2MnSn. Since $dM/dH \sim 1/J^*$, the Sn addition greatly reduces the exchange.

The strongly reduced intersublattice exchange has two consequences. First, it shifts the maximum of the THE peak towards lower fields, by a factor of about 2.4. Aside from this, Sn addition is likely to somewhat reduce the anisotropy, which would yield an additional shift. Second, Eq. (10) can be used to estimate the *height* of the THE peak. With Eqs. (6) and (8a), it leads to the dependence $\rho_{xy}(max) \sim 1/J^{*3/2}$. Comparison of $Ru_2Mn_{0.8}Sn_{1.2}$ and Ru_2MnSn yields a factor of about 13, which is consistent with the much stronger THE signal of the Mn-poor alloy.

Further support for the above scenario is provided by the magnetoresistance data of Fig. 5. As explained above, $Ru_2Mn_{0.8}Sn_{1.2}$ can be characterized as a diluted antiferromagnet containing uncompensated spin clusters, although its MR signature is (weakly) ferromagnetic. This behavior is ascribed to the alignment of the direction of $\boldsymbol{M}$ in the external magnetic field, as schematically depicted in Fig. 8(d).

The above model provides a basic explanation of THE but is only semiquantitative. First, the precise spin structure of the sample is largely unknown, except that there is very likely (almost certainly) a spin inhomogeneity of the type shown in Fig. 8(d). It is unclear, for example, whether $\boldsymbol{M}$ forms skyrmions [32] or exhibits a spatial variation that reflects the magnetization history and leads to magnetic bubbles [35]. This will replace our $\boldsymbol{M}_1 \cdot (\boldsymbol{M}_2 \times \boldsymbol{M}_3)$ estimate by a more precise spin distribution. Second, the AFM states of Ru_2MnSn and $Ru_2Mn_{0.8}Sn_{1.2}$ are only partially characterized. Further, Ru_2MnSn sample contains a feature that probably reflects small ferromagnetic impurity (see above), and the low signal strength further complicates the evaluation of THE in Fig. 7. Concerning $Ru_2Mn_{0.8}Sn_{1.2}$, we do not have an authoritative explanation of the $M(T)$ behavior, Fig. 4(a), aside from understanding the overall magnitude of M. One reason may be the interference of hysteretic effects, as indicated by the red curve in Fig. 4(b). Third, the micromagnetic description of the spin structure is only qualitative. Equation (2) describes a cubic crystal structure by uniaxial anisotropy. Both anisotropies yield similar spin inhomogeneities $\boldsymbol{M}(\boldsymbol{r})$, but the random-anisotropy averaging is quantitatively different. Similarly, the intra- and interatomic exchange stiffnesses [37] are not included, which basically amounts to the neglect of domain-wall motion.

In brief, we ascribe the THE of Ru_2MnSn and $Ru_2Mn_{0.8}Sn_{1.2}$ to the antiferromagnetic structure of the alloys. The THE signal is very clear, especially in $Ru_2Mn_{0.8}Sn_{1.2}$, and explained by a scissor mode in combination with polycrystalline anisotropy. The height and position of the THE maximum strongly decrease with increasing AFM intersublattice exchange J*, which is readily obtained from the experimental high-field susceptibility $dM/dH \sim 1/J^*$. Compared to Ru_2MnSn, $Ru_2Mn_{0.8}Sn_{1.2}$ has a strongly reduced J* and therefore a strongly enhanced THE. The scissor mode is also seen in the magnetoresistance: $Ru_2Mn_{0.8}Sn_{1.2}$ is an AFM but exhibits a FM-like negative magnetoresistance, ascribed to a net magnetic moment associated with the scissor mode.

The antiferromagnetic scissor mode is of great current interest in spin electronics for data information processing [38–40], because its frequencies are in the THz region, compared to the GHz frequencies of the propeller mode. The manipulation of the scissor mode is therefore an important issue, and in the present case, a rapidly varying magnetic field creates a rapid topological Hall response.

A very simple explanation of the difference between Ru_2MnSn and $Ru_2Mn_{0.8}Sn_{1.2}$, corroborated by the detailed discussion above, is as follows. The THE increases with the net magnetization $\boldsymbol{M}(\boldsymbol{r})$, Fig. 8(d), and this magnetization is created by the magnetic field. In fact, the perpendicular AFM magnetization of Fig. 4(b) is almost equal to $\boldsymbol{M}(\boldsymbol{r})$. Comparing the slopes of the red and green curves in Fig. 4(b) shows that $\boldsymbol{M}(\mathbf{r})$ is much bigger for the Mn-poor alloy than for the stoichiometric alloy, explaining the substantially enhanced THE signal.

4. Conclusions

We have fabricated $Ru_2Mn_{1.2}Sn_{0.8}$, Ru_2MnSn, and $Ru_2Mn_{0.8}Sn_{1.2}$ alloys, and investigated their magnetic and spin-electronic properties. The alloys crystallize in the $L2_1$ Heusler structure and exhibit drastic changes in the magnetic properties as a function of Sn content. While $Ru_2Mn_{1.2}Sn_{0.8}$ has a Curie temperature $T_c = 310$ K and a spontaneous magnetization of 2.52 μ_B per formula unit, Ru_2MnSn is antiferromagnetic with a Néel temperature above room temperature. Magnetization data indicate that the magnetic structure of $Ru_2Mn_{0.8}Sn_{1.2}$ is similar to a diluted antiferromagnet which has localized regions or clusters of uncompensated Mn spins caused by Mn deficiency. $Ru_2Mn_{0.8}Sn_{1.2}$ shows a negative magnetoresistance, and a pronounced topological Hall effect, which is explained by a new model considering a spatially varying noncoplanar scissor mode. This research on antiferromagnetic spin structures may be important for future THz information processing.

5. Authors' contributions

W.Z. fabricated and characterized the samples. W.Z., B.B., R.S., and D.J.S. analyzed the data and wrote the manuscript. Y.S., C.Z., and K.M. performed the DFT calculations. R.S and A.U. developed the analytical model. R.P. assisted the sample-fabrication process. S.R.V contributed towards the structural analysis using X-ray diffraction. X.Z.L. assisted the TEM measurements and analysis. D.J.S. supervised the project. All authors read and approved the final manuscript.

Declaration of Competing Interest

The authors declare that they have no known competing financial interests or personal relationships that could have appeared to influence the work reported in this paper.

Acknowledgement

This work is supported by the U.S. National Science Foundation - Designing Materials to Revolutionize and Engineer our Future: Sustainable Chemistry, Engineering, and Materials (NSF-DMREF: SusChEM) under the grant numbers 1729288 (synthesis and characterization) and 1729677 (DFT calculations) and the U.S. Department of Energy (DOE) under the award number DE-FG02-04ER46152 (analytical calculations). Research at Nebraska was performed in part in the Nebraska Nanoscale Facility: National Nanotechnology Coordinated Infrastructure and the Nebraska Center for Materials and Nanoscience (and/or NERCF), which are supported by the National Science Foundation under Award ECCS: 2025298, and the Nebraska Research Initiative.

References

[1] T. Jungwirth, X. Marti, P. Wadley, J. Wunderlich, Nature Nanotech. 11 (2016) 231.
[2] V. Baltz, A. Manchon, M. Tsoi, T. Moriyama, T. Ono, Y. Tserkovnyak, Rev. Modern Phys. 90 (2018), 015005.
[3] S. Fukami, V.O. Lorenz, O. Gomonay, J. Appl. Phys. 128 (2020), 070401.
[4] C. Sürgers, G. Fischer, P. Winkel, H. von Löhneysen, Nat. Commun. 5 (2014) 3400.
[5] S. Zhang, S. Xia, Q. Cao, D. Wang, R. Liu, Y. Du, Appl. Phys. Lett. 115 (2019), 022404.
[6] J.J. Nakane, K. Nakazawa, H. Kohno, Phys. Rev. B 101 (2020), 174432.
[7] J.M. Taylor, A. Markou, E. Lesne, P.K. Sivakumar, C. Luo, F. Radu, P. Werner, C. Felser, S.S.P. Parkin, Phys. Rev. B 101 (2020), 094404.
[8] P.K. Rout, P.V.P. Madduri, S.K. Manna, A.K. Nayak, Phys. Rev. B 99 (2019), 094430.
[9] B. Göbel, A. Mook, J. Henk, I. Mertig, Phys. Rev. B 96 (2017) 060406(R).
[10] W. Legrand, D. Maccariello, F. Ajejas, S. Collin, A. Vecchiola, K. Bouzehouane, N. Reyren, V. Cros, A. Fert, Nat. Mater. 19 (2020) 34.
[11] N. Nagaosa, Y. Tokura, Nat. Nanotechnol. 8 (2013) 899.
[12] B. Balasubramanian, P. Manchanda, R. Pahari, Z. Chen, W. Zhang, S.R. Valloppilly, X. Li, A. Sarella, L. Yue, A. Ullah, P. Dev, D.A. Muller, R. Skomski, G. C. Hadjipanayis, D.J. Sellmyer, Phys. Rev. Lett. 124 (2020), 057201.
[13] L. Wollmann, A.K. Nayak, S.S.P. Parkin, C. Felser, Ann. Rev. Mater. Res. 47 (2017) 247.

[14] K. Manna, Y. Sun, L. Muechler, J. Kübler, C. Felser, Nature Rev. Mater. 3 (2018) 244.
[15] S. Sanvito, C. Oses, J. Xue, A. Tiwari, M. Zic, T. Archer, P. Tozman, M. Venkatesan, J.M.D. Coey, S. Curtarolo, Sci. Adv. 3 (2017), e1602241.
[16] T. Suzuki, R. Chisnell, A. Devarakonda, Y.-T. Liu, W. Feng, D. Xiao, J.W. Lynn, J. G. Checkelsky, Nat. Phys. 12 (2016) 1119.
[17] R. Saha, A.K. Srivastava, T. Ma, J. Jena, P. Werner, V. Kumar, C. Felser, S.S. P. Parkin, Nat. Commun. 10 (2019) 5305.
[18] I. Galanakis, P.H. Dederichs, Phys. Rev. B 66 (2002), 174429.
[19] T. Kanomata, M. Kikuchi, H. Yamauchi, J. Alloy Comp. 414 (2006) 1.
[20] W.Y. Zhang, B. Balasubramanian, P. Kharel, R. Pahari, S.R. Valloppilly, X.Z. Li, L. Yue, R. Skomski, D.J. Sellmyer, APL Mater. 7 (2019), 121111.
[21] B. Balasubramanian, M. Sakurai, C.-Z. Wang, X. Xu, K.-M. Ho, J. Chelikowsky, D. J. Sellmyer, Mol. Syst. Des. Eng. 5 (2020) 1098.
[22] P.E. Blöchl, Phys. Rev. B 50 (1994) 17953.
[23] a) G. Kresse, J. Furthmüller, Comput. Mater. Sci. 6 (1996) 15;
b) G. Kresse, J. Furthmüller, Phys. Rev. B 54 (1996) 11169.
[24] J.P. Perdew, K. Burke, M. Ernzerhof, Phys. Rev. Lett. 77 (1996) 3865.
[25] H.J. Monkhorst, J.D. Pack, Phys. Rev. B 13 (1976) 5188.
[26] Y. Takamura, R. Nakane, S. Sugahara, J. Appl. Phys.. 105 (2009) 07B109.
[27] X.-Z. Li, SAED3: simulation and analysis of electron diffraction patterns in Microscopy and Analysis, May issue (2019) 16–19.
[28] S. Singh, S.W. D'Souza, J. Nayak, E. Suard, L. Chapon, A. Senyshyn, V. Petricek, Y. Skourski, M. Nicklas, C. Felser, S. Chadov, Nat. Commun. 7 (2016) 12671.
[29] H. Yamada, S. Takada, Progress Theor. Phys. 48 (1972) 1828.
[30] (a) H. Yamada, S. Takada, J. Phys. Soc. Jpn. 34 (1993) 51;
(b) C. Mazumdar, A.K. Nigam, R. Nagarajan, L.C. Gupta, G. Chandra, B.D. Padalia, C. Godart, R. Vijayaraghaven, J. Appl. Phys. 81 (1997) 5781.
[31] S.X. Huang, C.L. Chien, Phys. Rev. Lett. 108 (2012), 267201.
[32] A. Hrabec, J. Sampaio, M. Belmeguenai, I. Gross, R. Weil, S.M. Chérif, A. Stashkevich, V. Jacques, A. Thiaville, S. Rohart, Nat. Commun. 8 (2017) 15765.
[33] W. Zhang, B. Balamurugan, A. Ullah, R. Pahari, X. Li, L. Yue, S.R. Valloppilly, A. Sokolov, R. Skomski, D.J. Sellmyer, Appl. Phys. Lett. 115 (2019), 172404.
[34] D. Xiao, M.-C. Chang, Q. Niu, Rev. Mod. Phys. 82 (2010) 1959.
[35] S. Seki, M. Mochizuki, Skyrmions in Magnetic Materials, Springer International, Switzerland, 2016.
[36] S. Chikazumi, Physics of Magnetism, Wiley, New York, 1964.
[37] J. Richter, R. Skomski, Phys. Stat. Sol (B) 153 (1989) 711.
[38] P. Stremoukhov, A. Safin, M. Logunov, S. Nikitov, A. Kirilyuk, J. Appl. Phys. 125 (2019), 223903.
[39] R. Skomski, A. Ullah, B. Balasubramanian, D.J. Sellmyer, J. Magn. Magn. Mater. 502 (2020), 166279.
[40] M.B. Jungfleisch, W. Zhang, A. Hoffmann, Phys. Lett. A 382 (2017) 865.